Elliptic and zigzag instabilities on co-rotating vertical vortices in a stratified fluid

Pantxika Otheguy, Jean-Marc Chomaz, Paul Billant

▶ To cite this version:

HAL Id: hal-01023354

https://hal-polytechnique.archives-ouvertes.fr/hal-01023354

Submitted on 28 Jul 2014

Elliptic and zigzag instabilities on co-rotating vertical vortices in a stratified fluid

By PANTXIKA OTHEGUY†, JEAN-MARC CHOMAZ
AND PAUL BILLANT

LadHyX, CNRS, École Polytechnique, F-91128 Palaiseau Cedex, France

We present a three-dimensional linear stability analysis of a couple of co-rotating vertical vortices in a stratified fluid. When the fluid is non-stratified, the two vortices are unstable to the elliptic instability owing to the elliptic deformation of their core. These elliptic instability modes persist for weakly stratified flow: $F_h > 10$, where F_h is the horizontal Froude number ($F_h = \Gamma_b/\pi a_b^2 N$ where Γ_b is the circulation of the vortices, a_b their core radius and N the Brunt–Väisälä frequency). For strong stratification ($F_h < 2.85$), a new zigzag instability is found that bends each vortex symmetrically with almost no internal deformation of the basic vortices. This instability may modify the vortex merging since at every half-wavelength along the vertical, the vortices are alternatively brought closer, accelerating the merging, and moved apart, delaying the merging. The most unstable vertical wavelength λ_m of this new instability is shown to be proportional to $F_h b_b$, where b_b is the distance between the vortices, implying that λ_m decreases with increasing stratification. The maximum growth rate, however, is independent of the stratification and proportional to the strain $S = \Gamma_b/2\pi b_b^2$. These scaling laws and the bending motion induced by this instability are similar to those of the zigzag instability of a counter-rotating vortex pair in a stratified fluid.

1. Introduction

Geophysical flows often exhibit stable stratification which limits vertical displacements and favours the formation of a layered structure. Horizontal layers have been identified in the atmosphere (Dalaudier *et al.* 1994; Cho, Jurgens & Slade 1996; Muschinski & Wode 1997; Thouret *et al.* 2000; Luce, Crochet & Dalaudier 2001), in the oceans (Dugan 1984; Gregg 1987) and in lakes (Thorpe 1977; Imberger & Ivey 1991). Laboratory experiments of stratified turbulence generated by towing a vertical rod (Park, Whitehead & Gnanadeskian 1994), or a rake of vertical bars (Fincham, Maxworthy & Spedding 1996; Holford & Linden 1999; Praud, Fincham & Sommeria 2005) as well as direct numerical simulations of stratified turbulence (Riley, Metcalfe & Weissman 1981; Herring & Métais 1989; Riley & Lelong 2000; Godeferd & Staquet 2003; Waite & Bartello 2004) also show the formation of layers, in which energy dissipation is mostly achieved by the strong vertical shear. The scaling of Riley *et al.* (1981) accounts for the fact that when the stratification is strong, the velocity field is mainly horizontal. These authors have further suggested that if both

† Present address: AZTI – Tecnalia, Herrera Kaia Portualdea z/g, 20110 Pasaia, Guipúzcoa, Spain.

the horizontal and the vertical length scales of the flow are large compared to the buoyancy length scale U/N (where U is the horizontal velocity scale and N the Brunt–Väisälä frequency), the leading-order dynamics are two-dimensional. Using this result, Lilly (1983) has proposed that the kinetic energy spectrum observed in the atmosphere at mesoscale is a manifestation of two-dimensional dynamics with an inverse cascade of energy from small ($\sim 1\,\text{km}$) to large ($\sim 500\,\text{km}$) scales. Cho & Lindborg (2001) have contradicted this interpretation and have shown that the energy cascade is in the downscale direction by computing high-order statistical moments of airborne turbulence measurements. Billant & Chomaz (2001) and Lindborg (2002) have proposed that the dynamics are not two-dimensional because the vertical length scale selected by the flow is the local buoyancy length scale U/N, invalidating the hypothesis of Riley *et al.* (1981) of a vertical length scale large compared to U/N.

In the particular case of a counter-rotating vortex pair, Billant & Chomaz (2000*a*) have shown that an instability, referred to as the zigzag instability, is responsible for the formation of layers with a vertical scale proportional to the buoyancy length scale. However, co-rotating vortices are as frequently encountered in turbulent flows as counter-rotating vortices. Furthermore, pairing of like-signed vortices is believed to be a dominant process in two-dimensional turbulence and to account for both the upscale energy transfer and the downscale enstrophy cascade through filamentation. Therefore, it is important to investigate whether co-rotating vertical vortices in a stratified fluid are subject to a similar three-dimensional zigzag instability, which would imply that the pairing process and the inherent cascade could be substantially modified by stratification.

In the present paper, we show by a numerical stability analysis that for weak stratification, co-rotating vortices are subject to the elliptic instability (Kerswell 2002) as observed experimentally by Meunier & Leweke (2001) and described theoretically by Le Dizès & Laporte (2002). However, for strong stratification, a new instability affects co-rotating vortex pairs which tends to decorrelate the flow on the buoyancy length scale. Its growth rate scales as the external strain that each vortex induces on the other and we argue that this instability belongs to the zigzag type.

The paper is organized as follows. In §2, a quasi-steady two-dimensional solution is first obtained from a two-dimensional numerical simulation initialized by two co-rotating Gaussian vortices. In §3, the three-dimensional stability of this basic state is then determined using a linearized pseudospectral numerical code combined with a Krylov method. Section 4 describes the three-dimensional instabilities observed when the stratification is varied. The effects of the Reynolds number and of the ratio between the vortices core size and their separation distance are further investigated in §5. Finally, some consequences of the zigzag instability on vortex merging are discussed in the concluding section. The effect of planetary rotation on the zigzag instability is considered in a companion paper (Otheguy, Billant & Chomaz 2006).

2. Two-dimensional simulation

2.1. *Numerical method*

The initial vorticity field ω_0^f in the fixed laboratory frame consists of two identical co-rotating axisymmetric Lamb–Oseen vortices which have Gaussian vorticity distributions:

$$\omega_0^f = \frac{\Gamma_0}{\pi a_0^2}\left(\exp\left(-\frac{\left(x - \frac{1}{2}b_0\right)^2 + y^2}{a_0^2}\right) + \exp\left(-\frac{\left(x + \frac{1}{2}b_0\right)^2 + y^2}{a_0^2}\right)\right), \qquad (2.1)$$

where (x, y) are the Cartesian coordinates in the horizontal plane, Γ_0 is the initial circulation of each vortex, a_0 the initial vortex core size and b_0 the initial distance between the vortex centres.

The two vortices initially rotate around each other at the angular velocity $\Omega_0 = \Gamma_0/\pi b_0^2$. In the frame of reference rotating at the angular velocity Ω_0, the two-dimensional Navier–Stokes equations read:

$$\begin{cases} \dfrac{\partial \boldsymbol{u}}{\partial t} + \omega \boldsymbol{e}_z \times \boldsymbol{u} + \nabla \dfrac{\boldsymbol{u}^2}{2} + 2\Omega_0 \boldsymbol{e}_z \times \boldsymbol{u} = -\nabla p + \nu \Delta \boldsymbol{u}, \\ \nabla \cdot \boldsymbol{u} = \boldsymbol{0}, \end{cases} \tag{2.2}$$

where $\boldsymbol{u}$ is the velocity vector in the rotating frame, p the pressure, ω the vertical vorticity component in the rotating frame and ν the kinematic viscosity. The initial vorticity in the rotating frame is then $\omega_0 = \omega_0^f - 2\Omega_0$.

In order to solve these equations using a pseudospectral code, we have made a further decomposition. Indeed, the Fourier decomposition and the associated periodic boundary conditions require that the computed flow has no mean vorticity and therefore no circulation on the domain boundaries. As shown by Pradeep & Hussain (2004), such a periodic simulation of a flow with non-zero circulation can lead to partially incorrect results. A simple solution to circumvent this problem consists of treating separately the mean vorticity in the rotating frame $\bar{\omega} = (1/L_x L_y) \iint \omega \, \mathrm{d}x \, \mathrm{d}y$ (here equal to $2\Gamma_0/L_x L_y - 2\Omega_0$) and the associated solid body rotation $(\bar{\omega}/2)\boldsymbol{e}_z \times \boldsymbol{x}$ from the remaining periodic vorticity and velocity fields $(\omega_p, \boldsymbol{u}_p)$ which can be properly decomposed on a Fourier basis, i.e.

$$\left.\begin{aligned} \omega &= \bar{\omega} + \omega_p, \\ \boldsymbol{u} &= \tfrac{1}{2}\bar{\omega}\boldsymbol{e}_z \times \boldsymbol{x} + \boldsymbol{u}_p. \end{aligned}\right\} \tag{2.3}$$

Inserting this decomposition into (2.2) gives

$$\left.\begin{aligned} \dfrac{\partial \boldsymbol{u}_p}{\partial t} + (\omega_p + \bar{\omega} + 2\Omega_0)\boldsymbol{e}_z \times \left(\boldsymbol{u}_p + \tfrac{1}{2}\bar{\omega}\boldsymbol{e}_z \times \boldsymbol{x}\right) + \nabla\tfrac{1}{2}\boldsymbol{u}_p^2 &= -\nabla P + \nu \Delta \boldsymbol{u}_p, \\ \nabla \cdot \boldsymbol{u}_p &= \boldsymbol{0}, \end{aligned}\right\} \tag{2.4}$$

where $P = p + \tfrac{1}{2}((\bar{\omega}/2)\boldsymbol{e}_z \times \boldsymbol{x})^2 + \boldsymbol{u}_p \cdot ((\bar{\omega}/2)\boldsymbol{e}_z \times \boldsymbol{x})$. These equations are solved using a pseudospectral code adapted from that used by Delbende, Chomaz & Huerre (1998). The Fourier transform of a given function g is denoted by a hat:

$$\hat{\boldsymbol{g}}(k_x, k_y, t) = \iint \boldsymbol{g}(x, y, t) \exp(-\mathrm{i}(k_x x + k_y y)) \, \mathrm{d}x \, \mathrm{d}y, \tag{2.5}$$

where the wavenumber is $\boldsymbol{k} = (k_x, k_y)$. Eliminating the pressure and enforcing the incompressibility condition gives

$$\dfrac{\partial \widehat{\boldsymbol{u}}_p}{\partial t} = -P(\boldsymbol{k})\left[\widehat{(\omega_p + \bar{\omega} + 2\Omega_0)\boldsymbol{e}_z \times \left(\boldsymbol{u}_p + \tfrac{1}{2}\bar{\omega}\boldsymbol{e}_z \times \boldsymbol{x}\right)}\right] - k^2 \nu \widehat{\boldsymbol{u}}_p, \tag{2.6}$$

where $P(\boldsymbol{k}) = (\delta_{ij} - k_i k_j/k^2)\boldsymbol{e}_i \boldsymbol{e}_j$ is the projection operator on the solenoidal space. The cross-product $\mathscr{A} = (\omega_p + \bar{\omega} + 2\Omega_0)\boldsymbol{e}_z \times (\boldsymbol{u}_p + (\bar{\omega}/2)\boldsymbol{e}_z \times \boldsymbol{x})$ is evaluated in the physical space and then transformed to the spectral space. It is worth noting that even if the total velocity $\boldsymbol{u} = (\bar{\omega}/2)\boldsymbol{e}_z \times \boldsymbol{x} + \boldsymbol{u}_p$ is not periodic, the cross-product $\mathscr{A}$ fulfils the periodic boundary conditions since the absolute vorticity $\omega_p + \bar{\omega} + 2\Omega_0$ tends to zero outside the vortex cores. Thus, the decomposition (2.3) allows us to simulate properly a flow with non-zero circulation using a pseudospectral code. Time
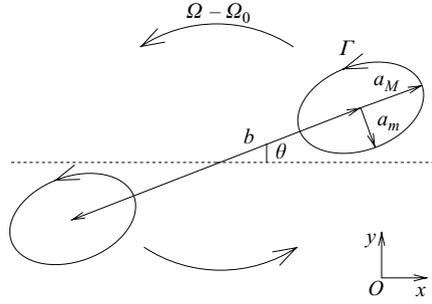
FIGURE 1. Sketch of the vortex pair evolution in the frame rotating at $\Omega_0 = \Gamma_0/\pi b_0^2$.

integration is performed with a second-order Adams–Bashforth scheme. Dissipative terms are integrated exactly. The 2/3 rule is applied for de-aliasing. The Reynolds number, defined as $Re_0 = \Gamma_0/\pi\nu$ is equal to 16 000. The size of the computational domain is chosen large enough, $L_x = L_y = 60a_0$ (i.e. 60 times the vortex radius), to minimize the effects of the periodic boundary conditions. The number of collocation points in the x and y directions is $M_x = M_y = 512$ in order to have a fine mesh ($\delta x = \delta y = 0.1172a_0$) in the vortex core and the time step is $\delta t = 0.01\pi a_0^2/\Gamma_0$.

2.2. *The two-dimensional evolution*

The time evolution of the vortex pair is analysed by fitting the vorticity ω by two elliptic Gaussian distributions separated by a distance b, with an instantaneous circulation Γ, a major semi-axis a_M and a minor semi-axis a_m (figure 1). The vortex core size is then $a = \sqrt{(a_M^2 + a_m^2)/2}$ and the eccentricity is $e = \sqrt{1 - (a_m/a_M)^2}$. The aspect ratio between the vortex core size and the separation distance between the vortices is defined as $\alpha = a/b$. This analytical vorticity field fits the simulated vorticity with an error typically less than 0.1 %. The vortex axis makes an angle θ with the x-axis. This angle is initially zero, but evolves very slowly at the rate $(\Omega - \Omega_0)$, where $\Omega = \Gamma/\pi b^2$, since computations are made in the frame rotating at the initial rotation rate of the vortex pair Ω_0. As described by Melander, Zabusky & McWilliams (1988), Le Dizès & Verga (2002), Meunier *et al.* (2002) and Cerretelli & Williamson (2003), the two-dimensional evolution of the vortices before merging exhibits three distinct phases. In the first inertial phase, each vortex deforms in order to adapt to the strain field generated by the other vortex. The vortex cores become elliptical on the inertial time scale $T_0 = \pi a_0^2/\Gamma_0$, with the major axis a_M aligned with the line joining the centres of the vortices. As seen in figure 2(*c*), the eccentricity makes a large jump at the very beginning of the simulation and rapidly relaxes towards equilibrium while exhibiting small and rapidly damped oscillations (barely visible in figure 2).

In the second viscous phase, the vortex pair remains quasi-steady with a distance b decreasing slowly (figure 2*a*). This implies that the vortices rotate in the computational domain since their mutual induction is no longer exactly compensated by the rotation of the reference frame. The small undulations with a long period just visible in figures 2(*a*) and 2(*b*) are artefacts of this late rotation of the vortices in a square box. The vortex radius evolves slowly by viscous diffusion according to the law (Batchelor 1967)

$$a = \sqrt{a_0^2 + 4\nu t}. \tag{2.7}$$

In this viscous phase, the eccentricity e increases almost linearly with time (figure 2*c*). Figure 2(*d*) shows also that e is a function of only $\alpha = a/b$ during this phase,
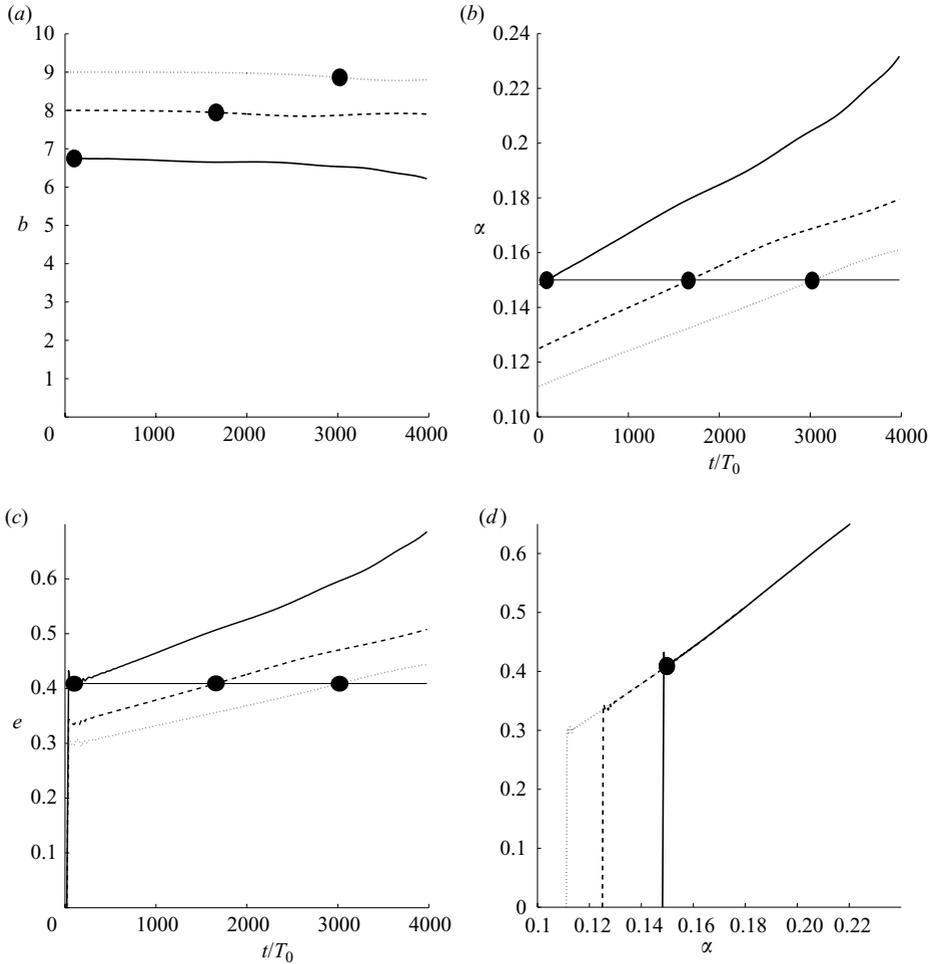
FIGURE 2. Time evolution of the characteristic parameters of the co-rotating vortex pair: (*a*) the separation distance b between the vortices; (*b*) the ratio $\alpha = a/b$ between the vortex radius a and the separation distance b; (*c*) the eccentricity e of one vortex. (*d*) Evolution of the eccentricity e as a function of α. The solid, dashed and dotted lines correspond to three simulations where α_0, the initial value of α, is respectively 0.148, 0.125 and 0.111. The other parameters of the simulation are: $M_x = M_y = 512$, $L_x = L_y = 60$, $a_0 = 1$, $Re_0 = 16\,000$. The filled circles represent the time where $\alpha = 0.15$, chosen for the stability analysis.

independently of the initial conditions. As analysed in detail by Sipp, Jacquin & Cossu (2000) and Le Dizès & Verga (2002), the vorticity distribution has relaxed towards a unique family of solutions parameterized by α. The two-dimensional basic state ($\boldsymbol{u}_b$, ω_b) for the following three-dimensional stability analysis (§ 3) is chosen in this regime for the particular aspect ratio $\alpha_b = a_b/b_b$ equal to 0.15 (filled symbols in figure 2). In the Appendix, we check that basic states with the same α_b, but computed from different initial α_0, have identical stability properties even if α_0 is very close to α_b (for example $\alpha_0 = 0.148$). The basic state with $\alpha_b = 0.15$ obtained from $\alpha_0 = 0.125$ will be used as the reference state for the stability analysis.

The final phase ends by the merging of the two vortices (not shown in figure 2) when α reaches the value 0.24 approximately (Le Dizès & Verga 2002).

3. Numerical method of the three-dimensional stability analysis

We now investigate the three-dimensional stability of the two-dimensional flow $(\boldsymbol{u}_b, \omega_b)$ corresponding to the instant where the parameter α has reached the desired value α_b. At this instant, the actual rotation rate of the two vortices differs slightly from Ω_0. Therefore, the three-dimensional stability computations are not done in the frame rotating at the velocity Ω_0, but in the frame rotating at the actual rotation rate Ω_b. For clarity, the notation has not been changed.

We consider that this basic state is embedded in a linearly stratified fluid with the mean density gradient aligned along the vortex axes. The total density ρ_t is expressed as the sum of a constant reference density ρ_0, a basic density profile $\bar{\rho}(z)$ and a perturbation density $\rho'(\boldsymbol{x}, t)$

$$\rho_t(\boldsymbol{x}, t) = \rho_0 + \bar{\rho}(z) + \rho'(\boldsymbol{x}, t). \tag{3.1}$$

The Brunt–Väisälä frequency $N = \sqrt{-(g/\rho_0)\,\mathrm{d}\bar{\rho}/\mathrm{d}z}$ is assumed to be constant.

In the following, space and time are, respectively, non-dimensionalized by the vortex radius a_b and by $\tau = \pi a_b^2/\Gamma_b$, the inverse of the vorticity at the centre of the vortex. The pressure is rescaled by $\rho_0(\Gamma_b/\pi a_b)^2$ and the density by $\rho_0\Gamma_b^2/g\pi^2 a_b^3$. We recall that a_b and Γ_b are the actual vortex radius and circulation determined by fitting the basic vorticity field by two elliptic Gaussian distributions. The same notation is kept for the non-dimensional variables for the sake of simplicity.

The basic state $(\boldsymbol{u}_b, \omega_b)$ is subjected to infinitesimal three-dimensional perturbations of the velocity $\boldsymbol{u}' = (u'_x, u'_y, u'_z)$, vorticity $\boldsymbol{\omega}' = \nabla \times \boldsymbol{u}'$, density ρ' and pressure p'. The linearized non-dimensional Navier–Stokes equations under the Boussinesq approximation in the frame rotating at Ω_b are:

$$\left.\begin{aligned}
\frac{\partial \boldsymbol{u}'}{\partial t} + \omega_b \boldsymbol{e}_z \times \boldsymbol{u}' + \boldsymbol{\omega}' \times \boldsymbol{u}_b + 2\Omega_b \boldsymbol{e}_z \times \boldsymbol{u}' &= -\nabla(p' + \boldsymbol{u}_b \cdot \boldsymbol{u}') - \rho'\boldsymbol{e}_z + \frac{1}{Re}\Delta\boldsymbol{u}', \\
\nabla \cdot \boldsymbol{u}' &= 0, \\
\frac{\partial \rho'}{\partial t} + \boldsymbol{u}_b \cdot \nabla\rho' - \frac{1}{F_h^2}u'_z &= \frac{1}{ScRe}\Delta\rho',
\end{aligned}\right\} \tag{3.2}$$

where $Sc = \nu/D$ is the Schmidt number, D being the molecular diffusivity of the stratifying agent, $Re = \Gamma_b/\pi\nu$ is the Reynolds number and the horizontal Froude number is defined as

$$F_h = \frac{\Gamma_b}{\pi a_b^2 N}. \tag{3.3}$$

As the basic state is uniform along the z-axis, the Fourier modes in the z-direction will not couple to each other and the perturbations can be written as follows:

$$[\boldsymbol{u}'; \boldsymbol{\omega}'; p'; \rho'](x, y, z, t) = [\boldsymbol{u}; \boldsymbol{\omega}; p; \rho](x, y, k_z, t)\exp(\mathrm{i}k_z z) + \mathrm{c.c.}, \tag{3.4}$$

where k_z is the vertical wavenumber and $c.c.$ denotes the complex conjugate.

A pseudospectral Gallerkin-collocation code similar to that described in §2.1 has been used to integrate equation (3.2) for each value of k_z. For that purpose, the complex perturbation $[\boldsymbol{u}; \boldsymbol{\omega}; p; \rho]$ corresponding to a particular value of k_z is decomposed in Fourier series in the horizontal directions as

$$[\boldsymbol{u}; \boldsymbol{\omega}; p; \rho](x, y, k_z, t) = \iint [\hat{\boldsymbol{u}}; \hat{\boldsymbol{\omega}}; \hat{p}; \hat{\rho}](k_x, k_y, k_z, t)\exp(\mathrm{i}(k_x x + k_y y))\,\mathrm{d}k_x\,\mathrm{d}k_y. \tag{3.5}$$

As in the two-dimensional case, equations (3.2) are projected onto the plane perpendicular to $\boldsymbol{k}$:

$$
\left.
\begin{aligned}
\frac{\partial \hat{\boldsymbol{u}}}{\partial t} &= P(\boldsymbol{k})[(\widehat{\boldsymbol{u} \times \omega_b}\boldsymbol{e}_z + \widehat{\boldsymbol{u}_b \times \boldsymbol{\omega}} - 2\Omega_b \boldsymbol{e}_z \times \hat{\boldsymbol{u}} - \hat{\rho}\boldsymbol{e}_z] - \frac{k^2}{Re}\hat{\boldsymbol{u}}, \\
\frac{\partial \hat{\rho}}{\partial t} &= -\mathrm{i}\boldsymbol{k} \cdot \widehat{\boldsymbol{u}_b \rho} + \frac{1}{F_h^2}\hat{u}_z - \frac{k^2}{ScRe}\hat{\rho},
\end{aligned}
\right\}
\tag{3.6}
$$

where $\boldsymbol{k} = (k_x, k_y, k_z)$. The products between the perturbation quantities and the basic state are evaluated in the physical space. The time step is $\delta t = 0.01$. The size of the computational domain and the number of collocation points are both halved compared to §2: $L_x = L_y = 30$, $M_x = M_y = 256$ in order to have a reasonable computational cost keeping the same resolution $\delta x = \delta y = 0.1172$. This is done either by running two-dimensional calculations in a $L_x = L_y = 30$ box or by cropping the basic state computed in the box $L_x = L_y = 60$ to a $L_x = L_y = 30$ box. In the Appendix, we show that these parameters give good accuracy and convergence of the numerical results. After integrating equation (3.6) for a sufficiently long time, typically $T = 500$ (i.e. 50 000 iterations with a time step equal to $\delta t = 0.01$), the most unstable eigenmode dominates the perturbation. The computation is generally initialized by divergence-free white noise. To speed up convergence time, the computation can also be initialized by an eigenmode already computed for another value of k_z. The results do not depend significantly on the initialization chosen.

In order to retrieve not only the most unstable eigenmode, but also the q most unstable eigenmodes, a Krylov method is applied (Edwards *et al.* 1994; Julien, Ortiz & Chomaz 2004). At the end of the simulation, the perturbation fields $\boldsymbol{u}'$ are saved at q distinct times separated by $\Delta T = 10$ time units. The vectors $U(T - j\Delta T)$, with $0 \leqslant j \leqslant q - 1$ are then orthonormalized to form the basis of a so-called Krylov subspace of dimension q, and we compute the eigenvalues of the evolution operator projected in this Krylov subspace.

4. Three-dimensional stability

Because of the central symmetry of the basic state with respect to the middle point between the vortex centres, the eigenmodes separate into two families: symmetric, defined by the same symmetry as the basic state,

$$
[u_x, u_y, u_z, \rho](x, y) = [-u_x, -u_y, u_z, \rho](-x, -y), \tag{4.1a}
$$

$$
[\omega_x, \omega_y, \omega_z](x, y) = [-\omega_x, -\omega_y, \omega_z](-x, -y). \tag{4.1b}
$$

and antisymmetric, defined by the opposite symmetry,

$$
[u_x, u_y, u_z, \rho](x, y) = [u_x, u_y, -u_z, -\rho](-x, -y), \tag{4.2a}
$$

$$
[\omega_x, \omega_y, \omega_z](x, y) = [\omega_x, \omega_y, -\omega_z](-x, -y). \tag{4.2b}
$$

In this section, the horizontal Froude number is varied in the range $[0.2, \infty]$, the Reynolds number $Re = 16\,000$, the Schmidt number $Sc = 1$, and the ratio $\alpha_b = 0.15$. We first present the elliptic instability which is observed for large Froude numbers $F_h > 10$. The zigzag instability, observed for small Froude numbers $F_h < 2.85$, will be described in §4.2.
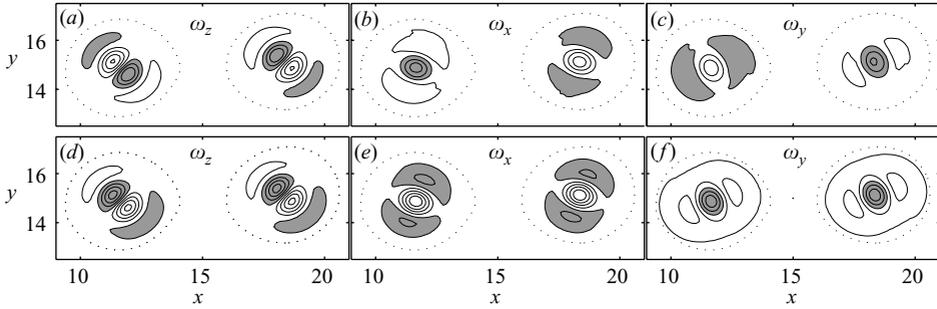
FIGURE 3. Contours of the three vorticity components of the elliptic instability: (a–c) symmetric mode and (d–f) antisymmetric mode for $k_z = 1.9$, $Re = 16\,000$ and $F_h = \infty$. The shaded regions indicate positive vorticity. The perturbation enstrophy has been normalized to one and the contour level is 0.013 for all the components except for the antisymmetrical ω_z (in (d)) for which it is 0.006. The dotted line superimposed is the vorticity isocontour 0.05 of the non-dimensional basic state vorticity.
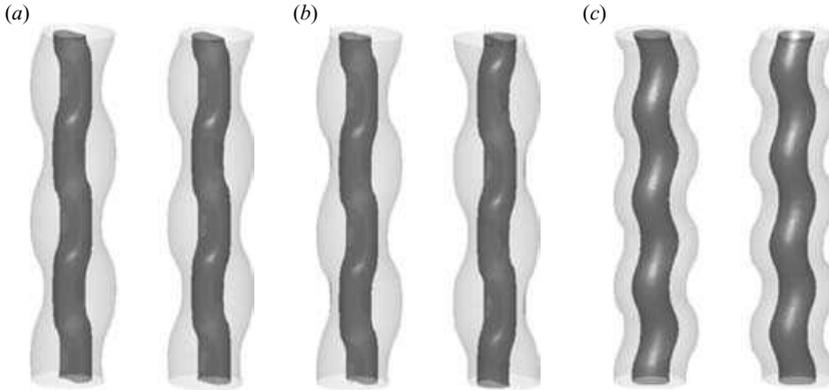

FIGURE 4. Vertical vorticity isosurfaces of the co-rotating vortex pair perturbed by (a) antisymmetric elliptic instability ($F_h = \infty$), (b) symmetric elliptic instability ($F_h = \infty$), (c) zigzag instability ($F_h = 0.5$). The elliptic instability corresponds to a deformation of the vortex core, whereas the zigzag instability is associated with a displacement of the vortex as a whole at each level z. The deformations have been obtained by adding to the basic flow the most unstable eigenmode with a small but finite amplitude. The black isosurfaces correspond to the vorticity value 50 % of the maximum vorticity, and transparent surfaces to 5 % of the maximum vorticity.

4.1. *Unstratified and weakly stratified flow* ($F_h > 10$)

For Froude numbers larger than 10, both symmetric and antisymmetric modes are unstable. The instability mechanism corresponds to the elliptic instability described by Moore & Saffman (1975) and Tsai & Widnall (1976) as the resonance between two Kelvin modes and the elliptic deformation of the vortex core. Figure 3 shows the perturbation vorticity field of the most unstable symmetric and antisymmetric modes in the non-stratified case ($F_h = \infty$). The vertical vorticity perturbation inside each vortex core is similar to the elliptic instability mode reported by Pierrehumbert (1986) and Waleffe (1990) with a dipole structure surrounded by a weak opposite vorticity (figure 3 a, d). This perturbation corresponds to a deformation of the vortex core in opposite phase to the vortex periphery as illustrated in figures 4(a) and 4(b).
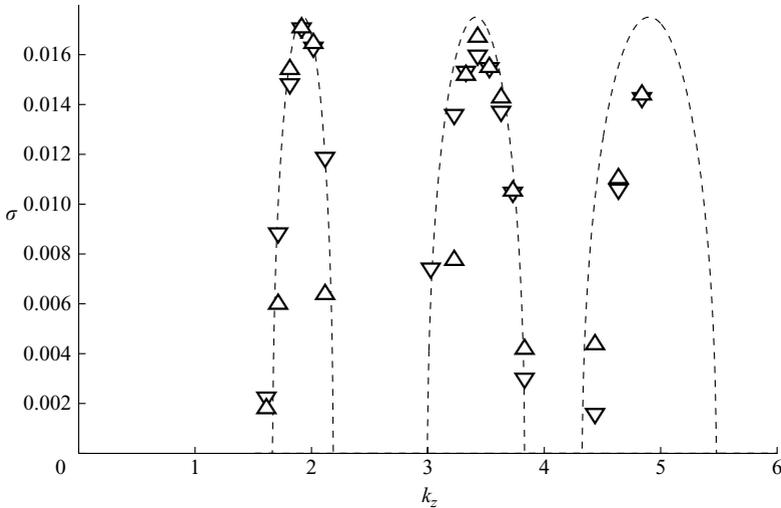
FIGURE 5. Plots of the growth rate of the elliptic instability as a function of the vertical wavenumber k_z for $Re = 16\,000$, $F_h = \infty$, and $\alpha_b = 0.15$. $\triangle$ and $\triangledown$ symbols show the growth rates of the symmetric and antisymmetric modes, respectively. The dash-dotted line represents the inviscid prediction of Le Dizès & Laporte (2002).

The x and y vorticity components of the perturbation are also displayed in figure 3 for later comparison with the zigzag instability. The growth rate of the symmetric and antisymmetric modes are shown in figure 5 as a function of the vertical wavenumber. In the range of wavenumbers investigated, three distinct bands of instability have been found for each mode. These bands correspond to the first three wavenumbers for which the resonance condition leading to the elliptic instability is satisfied (Tsai & Widnall 1976; Eloy & Le Dizès 1999). Our numerical results are in good agreement with the theoretical inviscid growth rate predicted by Le Dizès & Laporte (2002)†. In particular, the growth rate of the most unstable mode $\sigma_m = 0.01771$ at $k_z = 1.9$ obtained for $Re = 16\,000$ differs by only 2 % from the predicted inviscid value $\sigma = 0.01741$ and by 9 % from the growth rate measured in the large-eddy numerical simulation of Le Dizès & Laporte (2002). The symmetric and antisymmetric modes have approximately the same growth rates for most of the wavenumbers investigated as expected since α_b is small. Other weakly unstable modes have been identified. They are about four times less unstable than the elliptic modes and they will not be described here. The elliptic modes are stabilized in the presence of stratification in agreement with the theoretical studies of Miyazaki (1993), Miyazaki & Fukumoto (1992), Kerswell (2002) and Leblanc (2003). Kerswell (2002) and Leblanc (2003) have derived asymptotically the inviscid growth rate σ_a of the elliptic instability in a stratified and rotating fluid in the limit of small strain and for an unbounded uniform vortex. In this local approximation, the elliptic instability corresponds to the parametric forcing of inertial gravity waves by the external strain field as described by Kerswell (2002). Using the present definition of non-dimensional variables and the fact that the non-dimensional

† A misprint has been corrected in Le Dizès & Laporte (2002): b^2/a_i^2 should be replaced by b^4/a_i^4 in equations (6.1) and (6.2).
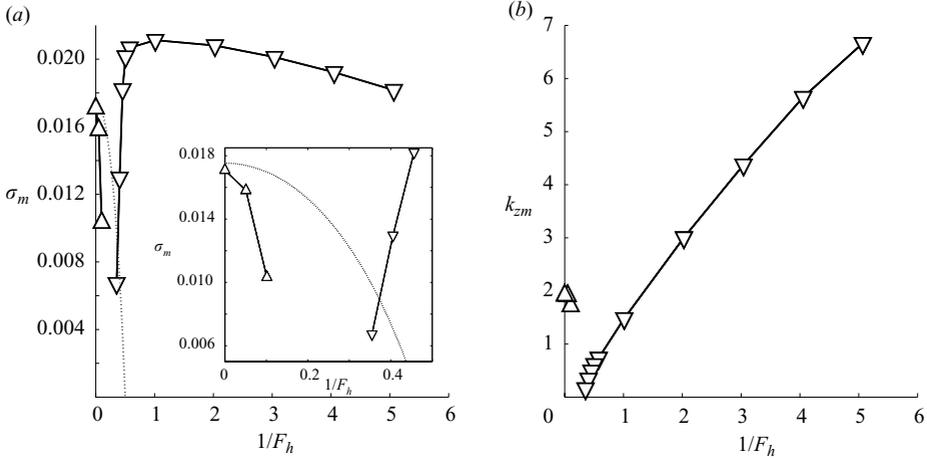
FIGURE 6. Evolution of (*a*) the maximum growth rate σ_m and (*b*) of the corresponding wavenumber k_{zm} as a function of the inverse of the horizontal Froude number for $Re = 16\,000$ and $\alpha_b = 0.15$. The symbols $\triangle$ and $\triangledown$ represent the elliptic and zigzag instabilities, respectively. The dotted line corresponds to the asymptotic value given by equation (4.3). A zoom on small $1/F_h$ is included in the inset (*a*).

rotation rate of the vortex pair is $\Omega_b = \alpha_b^2$, the asymptotic growth rate reads

$$\sigma_a = \frac{9}{16}\epsilon\frac{\left(3 + 4\alpha_b^2\right)^2\left(1 - 4/F_h^2\right)}{9\left[\left(1 + 2\alpha_b^2\right)^2 - 1/F_h^2\right]}, \tag{4.3}$$

where ϵ is the non-dimensional local strain rate.

For a Lamb–Oseen vortex, Le Dizès & Laporte (2002) have derived an approximation for the constant of proportionality between the local strain ϵ inside the vortex core and the external strain rate S imposed by the other vortex

$$\epsilon = \left(1.5 + 0.038\left(0.16 - \alpha_b^2\right)^{-9/5}\right)S, \tag{4.4}$$

where the non-dimensional external strain rate is according to our definitions $S = \alpha_b^2/2$. Consequently, the asymptotic growth rate can be expressed solely as a function of α_b and F_h. In the non-stratified case ($F_h = \infty$), and for $\alpha_b = 0.15$, equation (4.3) predicts an asymptotic growth rate $\sigma_a = 0.0175$, which is remarkably close to the maximum growth rate obtained numerically, $\sigma_m = 0.0171$, despite the fact that the vortex is bounded and not uniform and that this growth rate is observed at a finite k_z ($k_z = 1.9$) for which the local approximation is not valid.

The asymptotic formula (4.3) predicts that the growth rate of the elliptic instability decreases as the Froude number decreases and vanishes for $F_h \leqslant 2$. We have determined numerically the most unstable wavenumber k_{zm} (figure 6*b*) and the corresponding maximum growth rate σ_m (figure 6*a*) when the Froude number decreases keeping the Reynolds number constant. When F_h decreases, the maximum growth rate σ_m drops more abruptly than the asymptotic growth rate σ_a and vanishes beyond the threshold: $F_h < 10$, i.e. sooner than predicted by equation (4.3).

A possible explanation for this discrepancy is that the Lamb–Oseen vortex has a distributed vorticity profile while equation (4.3) pertains to a uniform and unbounded vorticity profile. The abrupt stabilization could be due to the presence of critical point singularities which may damp the Kelvin modes involved in the elliptic instability

when the fluid is stratified and the vorticity is distributed. As shown in the non-stratified case by Sipp & Jacquin (2003) and Le Dizès & Lacaze (2005), critical points occur for Kelvin modes of a Lamb–Oseen vortex at a radial location r_c where the local angular velocity $V_\theta(r_c)/r_c$ equals the azimuthal phase velocity w/m, where w is the mode frequency and m its azimuthal wavenumber. These waves are then damped in contrast to those of a uniform vortex. For the $m = 1$ Kelvin waves, the waves with a frequency in the band $0 < w < \Omega_{max}$ (where Ω_{max} is the maximum angular velocity) are damped. This damping does not affect the elliptic instability since the resonance between $m = \pm 1$ Kelvin waves occurs for $w = 0$. This explains to some extent why, in the non-stratified case, the growth rates of the elliptic instability for a uniform vortex and for the Lamb–Oseen vortex are very close. In contrast, the elliptic instability due to the resonance between the $m = 0$ and $m = 2$ Kelvin modes is observed for uniform vorticity (Rankine vortex) (Eloy & Le Dizès 1999) and not for distributed vorticity (Lamb–Oseen vortex) (Sipp & Jacquin 2003) since the $m = 2$ Kelvin mode at the resonant frequency exhibits a critical point and is damped in the case of the Lamb–Oseen vortex. We propose that a similar damping phenomenon occurs for the $m = \pm 1$ waves in the presence of stratification. Indeed, a critical point should occur when the local frequency $|w - m\Omega(r)|$ equals the Brunt–Väisälä frequency N. Therefore the range of frequencies where the Kelvin mode $m = +1$ has a critical point is extended to the range $-N < w < \Omega_{max} + N$. Thus, as soon as a weak stratification is present, the resonant $m = \pm 1$ waves of frequency $w = 0$ participating in the elliptic instability may have a singularity and be damped. This could explain why the growth rate pertaining to equation (4.3) for a uniform and unbounded vortex which predicts so well the instability growth rate for $N = 0$, no longer agrees with the numerical results when $N > 0$. A detailed analysis of the Kelvin mode structure of the Lamb–Oseen vortex in the presence of stratification would be necessary to prove this conjecture.

In the gap $2.85 < F_h < 10$, weakly unstable modes have been observed with a growth rate nearly four times smaller than the growth rate of the modes studied in the present paper. They will not be discussed here. For F_h lower than 2.85, a new mode appears which corresponds to the zigzag instability.

4.2. *Zigzag instability for $F_h < 2.85$*

As seen in figure 6, the maximum growth rate of the zigzag instability levels off abruptly for $F_h = 2.85$, reaches a value larger than the elliptic instability growth rate and then remains almost constant with decreasing F_h while the most unstable vertical wavenumber increases as $1/F_h$.

4.2.1. *A displacement mode*

The perturbation vorticity fields of the zigzag instability (figure 7) differ from those of the elliptic instability (figure 3). The horizontal vorticity components ω_x and ω_y are no longer confined in the vortex cores since the baroclinic torque can produce horizontal vorticity outside the vortex cores in contrast to the case of non-stratified fluids where horizontal vorticity may be produced only by tilting of the basic flow vorticity.

The vertical vorticity component ω_z continues to be localized in the vortex core (figure 7c) since it is either due to the transport of the basic flow vorticity or to the stretching of the basic flow vorticity, both tilting and baroclinic terms being only horizontal. The vertical vorticity field ω_z exhibits a single dipole that occupies the whole vortex core (dotted line in figure 7c) in contrast to the elliptic instability
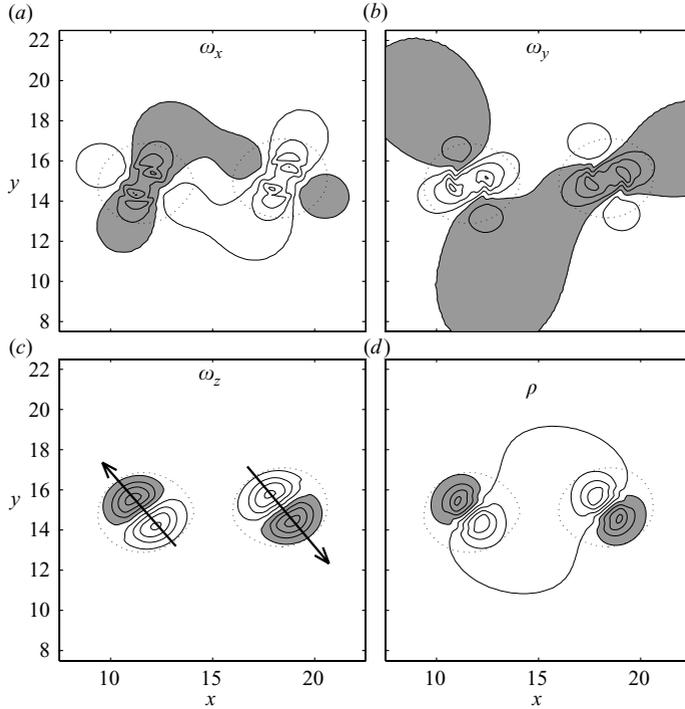
FIGURE 7. Contours of (*a*, *b*, *c*) the three vorticity components ω_x, ω_y, ω_z and (*d*) density field ρ of the zigzag instability for $F_h = 1$, $k_z = 1.5$ and $Re = 1000$. Shaded regions indicate positive value. The perturbation enstrophy has been normalized to one and the contour level of the three vorticity components is 0.007. The contour level of the density field is 0.028. The dotted line superimposed on the perturbation components is the isocontour 0.05 of the maximum basic state vorticity. The plain arrows in (*c*) indicate the directions of bending of the two vortices owing to the zigzag instability.

(figure 3*a*) for which a smaller dipole surrounded by opposite vorticity was observed. This eigenmode is symmetric, the antisymmetric mode is stable in contrast to the elliptic instability where both the symmetric and the antisymmetric modes were unstable. The deformations induced by the zigzag instability are very different from the deformations induced by the elliptic instability as illustrated in figure 4(*c*). The shape of the eigenmode within each basic vortex (figure 7*c*) resembles strongly the structure of the zigzag instability of a counter-rotating vortex pair in a stratified fluid (Billant & Chomaz 2000*c*). For the latter basic flow, it was shown that the zigzag eigenmode corresponds to a translation as a whole of each vortex with almost no internal deformation, which is equivalent to a bending of each vortex. In the present case, the dipolar shape of the vertical vorticity perturbation corresponds also to a uniform translation of each vortex. Indeed, figure 8 showing the perturbation associated with a uniform translation of one vortex of the basic state in an arbitrary direction θ has a striking resemblance to the pattern observed in each vortex in figure 7(*c*). The zigzag instability induces therefore mainly a bending of each vortex in opposite directions obliquely with an angle θ relative to the axis joining the vortex centres (figure 7*c*). This motion may be decomposed as a small rotation of the vortex pair and a variation of the distance between the vortices. We may anticipate that this instability will favour or delay the merging of the vortices alternately along the vertical since the vortices will be brought
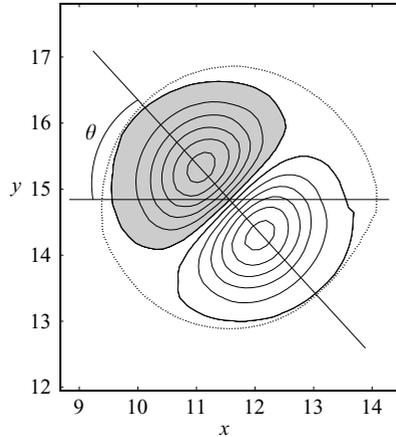
FIGURE 8. Vertical vorticity perturbation corresponding to an infinitesimal translation of one vortex of the basic state in the direction θ that is to say $\omega_z \propto (-\cos\theta(\partial/\partial x) + \sin\theta(\partial/\partial y))\omega_b$. For other details see the legend of figure 7.

closer or moved apart alternately along the vertical. The nonlinear evolution of the zigzag instability and its impact on the vortex merging will be reported in the future.

4.2.2. *Self-similarity of the growth rate of the zigzag instability*

The growth rate of the zigzag instability is shown in figure 9(a), as a function of the vertical wavenumber for various Froude numbers. A single bell-shaped curve is observed for each Froude number in contrast to the elliptic instability where several isolated peaks were present (figure 5). This curve is shifted toward larger vertical wavenumbers when the Froude number decreases, but the maximum growth rate remains almost constant. As will be shown later, the slight decrease for small Froude numbers is due to viscous effects which may be approximated by $(1/Re)k_z^2$ when k_z is large.

As observed in figure 6, the vertical wavenumber corresponding to the maximum growth rate of the zigzag instability increases as $1/F_h$. The growth rate curves of figure 9(a) are replotted in figure 9(b) as a function of the rescaled wavenumber $k_z F_h$. All the growth rates are seen to collapse in a single curve to a reasonable accuracy. When the viscous damping is taken into account by plotting $\sigma + (1/ReF_h^2)(k_z F_h)^2$ as a function of $k_z F_h$ (figure 9c), the collapse is even better. In particular, we notice that the lower the Froude number, the better the curves collapse. This indicates that the growth rate is of the form $\sigma = f(k_z F_h) - (1/ReF_h^2)(k_z F_h)^2$ for small Froude numbers in agreement with the self-similarity law proposed by Billant & Chomaz (2000b,c, 2001). In the inviscid limit, the non-dimensional vertical wavelength of the zigzag instability is proportional to the Froude number F_h, decreasing as the stratification increases, and the growth rate of this instability is independent of F_h. Because of viscous effects, the maximum growth rate decreases as $(1/ReF_h^2)$, and when ReF_h^2 is order unity, the zigzag instability should be inhibited by viscosity.

4.2.3. *Self-similarity of the eigenmode structure*

The self-similarity property also applies to the eigenmode structure. For a given value of $k_z F_h$, but with different values of F_h, the vertical vorticity perturbations are nearly identical, as shown in figure 10. The vertical vorticity perturbation exhibits a similar dipolar shape in each vortex core for all the wavenumbers and Froude
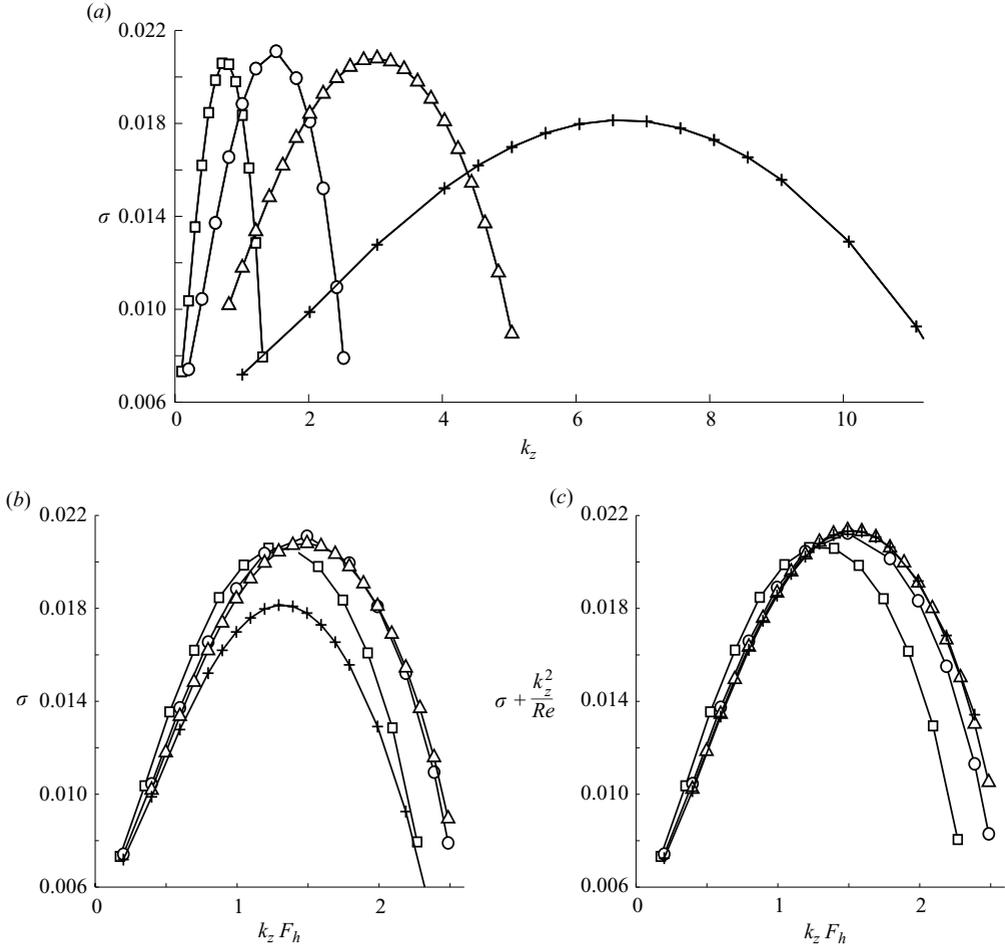
FIGURE 9. Plots of the growth rate of the zigzag instability for different low Froude numbers as a function of (a) the vertical wavenumber k_z, (b) the vertical wavenumber rescaled by the horizontal Froude number $k_z F_h$. In (c), the growth rate has been compensated for the viscous damping and plotted against $k_z F_h$. $\square$, $F_h = 1.7$; $\circ$, $F_h = 1$; $\triangle$, $F_h = 0.5$; $+$, $F_h = 0.2$. The Reynolds number is $Re = 16\,000$.

numbers. Only the orientation of the dipole varies with the rescaled wavenumber $k_z F_h$. This implies that the instability always consists of a translation, but the direction of the translation varies with $k_z F_h$. For small $k_z F_h$, the direction of translation of each vortex tends to be perpendicular to the line joining the vortex centres. This means that the instability consists mainly of a rotation as a whole of the vortex pair without change of the distance between the vortices. When $k_z F_h$ increases, the direction of translation rotates toward the x-axis implying that, in addition to the rotation of the vortex pair, there is a significant translation of the vortices along the x-axis in opposite directions.

5. Effects of the Reynolds number and of the ratio α_b on the zigzag instability

5.1. *The effect of the Reynolds number*

Figure 11(a) shows the effect of the Reynolds number on the zigzag instability for a moderate Froude number $F_h = 1$. The maximum growth rate and its corresponding
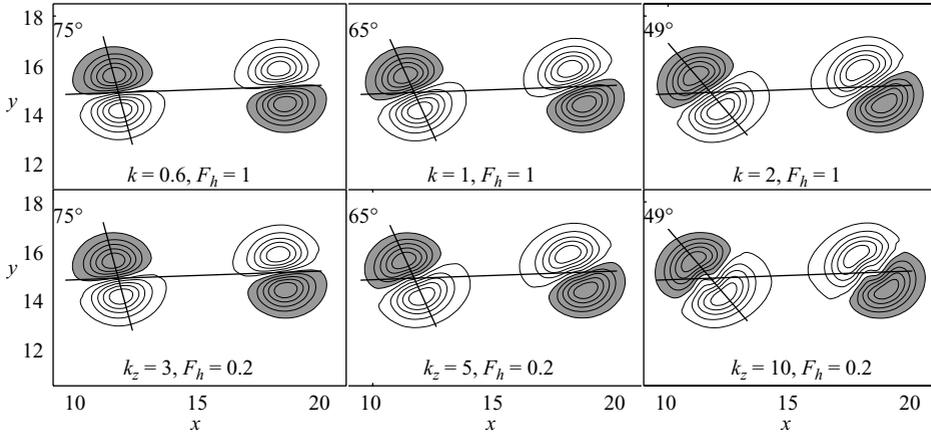
FIGURE 10. Evolution of the vertical vorticity of the eigenmode for two Froude numbers $F_h = 0.2$ and $F_h = 1$ and various wavenumbers such that $k_z F_h$ is equal to 0.6, 1 and 2, respectively, in the first, second and third columns. The Reynolds number is kept equal to 16 000. The orientation, of the dipolar shape in the left-hand vortex and the line joining the centres of the basic vortices are shown by solid lines. The angles between these two lines are noted on the top left-hand corner of each plot.
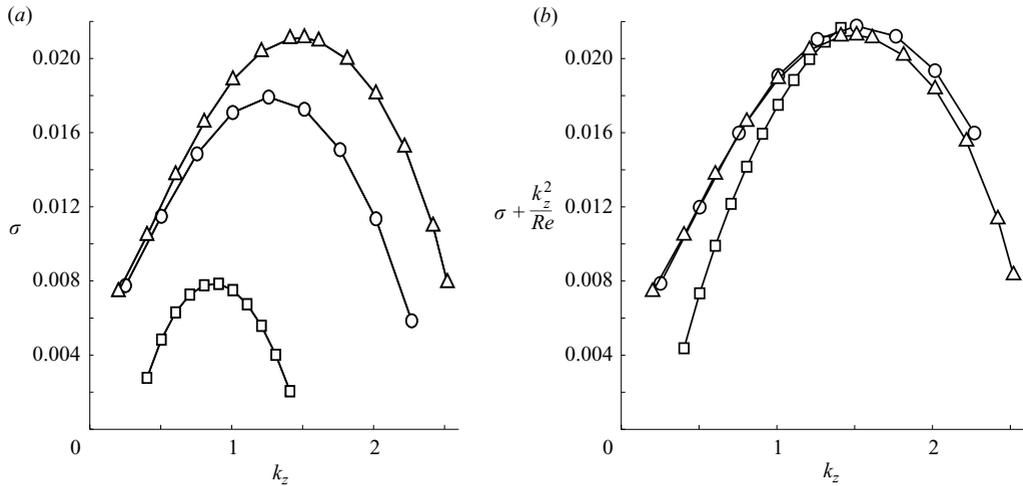

FIGURE 11. Plots of the growth rate of the zigzag instability for different Reynolds numbers: (a) growth rate as a function of k_z, (b) growth rate compensated for viscous damping against k_z. $\square$, $Re = 100$; $\bigcirc$, $Re = 500$; $\triangle$, $Re = 16\,000$. The Froude number is $F_h = 1$.

wavenumber decrease as the Reynolds number decreases. In particular, the maximum growth rate is reduced by a factor of two when the Reynolds number is decreased from $Re = 500$ to $Re = 100$. The most unstable wavenumber also decreases slightly. If, as in figure 9, we compensate the growth rate by the vertical viscous diffusion $\sigma + k_z^2/Re$ (figure 11b), the three curves collapse satisfactorily, showing that the zigzag instability is mainly affected by vertical viscous diffusion even for this moderate value of the Froude number.
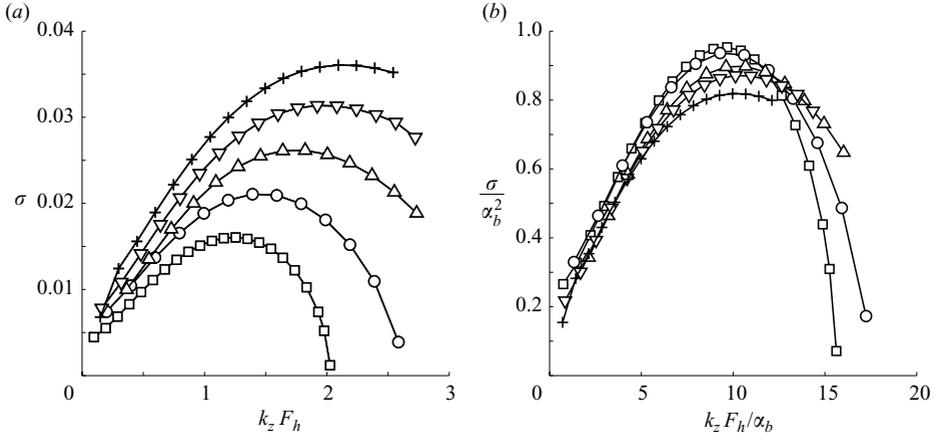
FIGURE 12. Plots of the growth rate of the zigzag instability for various values of α_b: (*a*) growth rate against wavenumber times F_h, (*b*) rescaled growth rate σ/α_b^2 against rescaled wavenumber $k_z F_h/\alpha_b$. $\square$, $\alpha_b = 0.13$, $F_h = 0.93$; $\bigcirc$, $\alpha_b = 0.15$, $F_h = 1$; $\triangle$, $\alpha_b = 0.17$, $F_h = 0.83$; $\bigtriangledown$, $\alpha_b = 0.19$, $F_h = 0.63$; $+$, $\alpha_b = 0.21$, $F_h = 0.55$. The Reynolds number is $Re = 16\,000$.

5.2. *The effect of the ratio* $\alpha_b = a_b/b_b$.

Figure 12(*a*) displays the growth rate of the zigzag instability for $Re = 16\,000$ for different ratios between the vortices core size and their separation distance α_b of the basic state. The Brunt–Väisälä frequency is kept constant. Since a_b varies, the Froude number also varies in the range [0.55,1]. A single bell-shaped curve is observed for each ratio α_b with a maximum growth rate σ_m and a most amplified rescaled wavenumber $k_{zm}F_h$ which both increase when α_b increases.

Figure 12(*b*) shows the growth rate of the zigzag instability rescaled by α_b^2 as a function of the wavenumber rescaled by F_h/α_b. We observe that the curves essentially collapse on a single curve demonstrating that the growth rate scales as twice the strain $S = \alpha_b^2/2$ while the most unstable wavenumber scales as α_b/F_h. The growth rate of the zigzag instability is proportional to the strain similarly to the elliptic instability (Tsai & Widnall 1976; Pierrehumbert 1986) and the Crow instability (Crow 1970) of a counter-rotating vortex pair. The most unstable wavenumber of the zigzag instability increases as α_b, meaning that its wavelength scales on the distance b_b between the two vortices since k_z was non-dimensionalized by a_b. This is similar to the Crow (1970) instability and in sharp contrast to the elliptic instability for which the wavelength scales on the vortex radius a_b and is independent of the distance b_b. These scaling properties will be explained by an asymptotic analysis in the spirit of Billant & Chomaz (2000*b*) in a forthcoming article.

6. Summary and conclusions

A pair of co-rotating vertical vortices in a stratified fluid is subjected to distinct three-dimensional instabilities depending on the Froude number. For $F_h > 10$, the celebrated elliptic instability is observed. Strikingly, its growth rate decreases more abruptly than predicted for an unbounded and uniform elliptical vortex (Kerswell 2002). A possible explanation is that the waves participating in the elliptic instability for a Gaussian vortex have a singularity and are damped in the presence of stratification.

For $F_h < 2.85$, a new three-dimensional instability has been found. The numerical stability analysis shows that this instability bends the vortices like the zigzag instability reported by Billant & Chomaz (2000*a*) on a counter-rotating vortex pair in a stratified fluid. In the present case, the shape of the eigenmode shows that the instability consists of an oblique translation of each vortex in opposite directions. This motion may be decomposed into a rotation as a whole of the vortex pair and a variation of the distance between the vortex centres. This instability may modify the vortex merging since at every half wavelength the vortices are alternatively brought closer, accelerating the merging, and moved apart, delaying the merging.

For a given value of the ratio α_b, we have shown that the wavelength of the zigzag instability is proportional to the Froude number while its growth rate is independent of F_h. Alternatively, for different ratios α_b, we have found that the wavelength of the zigzag instability scales as F_h/α_b while its growth rate scales as α_b^2. The dimensional vertical wavelength selected by the zigzag instability is therefore proportional to $F_h b_b$, which corresponds to the buoyancy length $L_B = \Gamma_b/\pi a_b N$ multiplied by b_b/a_b. It decreases for increasing stratification. The maximum dimensional growth rate is proportional to the strain $\Gamma_b/2\pi b_b^2$, i.e. independent of N as in the case of two counter-rotating vortices (Billant & Chomaz 2000*c*). It is worth emphasizing that its maximum growth rate is slightly larger than that of the elliptic instability in a non-stratified fluid.

Under the assumption that the vertical length scale is large compared to the buoyancy length scale L_B, strongly stratified flows are often thought to behave as two-dimensional flows (Riley *et al.* 1981; Lilly 1983; Riley & Lelong 2000). However, since the vertical scale selected by the zigzag instability is of the order of the buoyancy length, the assumption at the root of the two-dimensional paradigm is not tenable. On the contrary, the present result confirms that stratified flows have a fully three-dimensional dynamics (Billant & Chomaz 2001; Lindborg 2002).

The existence of the zigzag instability on both co-rotating and counter-rotating vortex pairs suggests that it is a generic instability which may affect stratified flows containing at least two vortices. This instability could explain why stratified turbulence (Herring & Métais 1989; Fincham *et al.* 1996; Riley & Lelong 2000; Godeferd & Staquet 2003; Waite & Bartello 2004) and more generally geophysical turbulence (Dugan 1984; Gregg 1987; Dalaudier *et al.* 1994; Lindborg 2002) exhibit a layered structure. Stratified flows experiments (Park *et al.* 1994; Holford & Linden 1999) and numerical simulations (Lindborg 2006; Waite & Bartello 2004) initially coherent on the vertical, exhibit layers with a thickness of the order of the buoyancy length in agreement with the scaling law of the wavelength of the zigzag instability. However, it is still to be confirmed that the zigzag instability is the mechanism which imposes this scaling law.

Appendix. Computational accuracy

In order to check the accuracy and convergence of the numerical results, we consider as a reference the parameter set: $M_x = M_y = 256$, $L_x = L_y = 30$, $\delta t = 0.01$, $a_0 = 1$, $b_0 = 6.75$ (we recall that the subscript 0 denotes the initial parameters of

1	2	3	4	5
Ref. case	$\Delta t = 0.005$	$M_x = M_y = 512$	$L_x = L_y = 60$	$\Omega_b = \Omega_0$
$\sigma = 0.01883$	$\sigma = 0.01887$	$\sigma = 0.01888$	$\sigma = 0.01815$	$\sigma = 0.01921$

TABLE 1. Check of the computational accuracy of the growth rate with respect to the numerical parameters for the same physical parameters $k_z = 1$, $\alpha_b = 0.15$, $Re = 16\,000$, $F_h = 1$. See the text for detailed explanations.
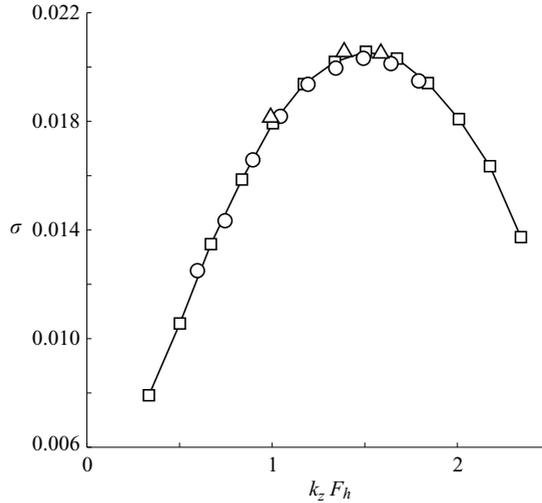

FIGURE 13. Plots of the growth rate as a function of the wavenumber times F_h for various initial distances between the vortices, $\triangle$, $b_0 = 6.75$, $F_h = 1$; $\square$, $b_0 = 8$, $F_h = 0.7$; $\bigcirc$, $b_0 = 9$, $F_h = 0.55$. The other parameters are kept constant: $M_x = M_y = 512$, $L_x = L_y = 60$, $\alpha_b = 0.15$, $Re = 16\,000$.

the two-dimensional simulation), $\alpha_b = 0.15$, $k_z = 1$, $Re = 16\,000$, $F_h = 1$. With these parameters, the growth rate has been found to be $\sigma = 0.01883$.

We have performed several tests to check the accuracy and the convergence of this result as given in table 1. Dividing the time step Δt by 2 (column 2), or doubling the number of collocation points M_x, M_y (column 3) changes the value of the growth rate by less than 1 %.

Table 1 (column 4) shows that widening the domain to $L_x = L_y = 60$ and keeping the same resolution has a little more influence and changes by about 3 % the growth rate value. Similarly, cropping the basic state computed in the box $L_x = L_y = 60$ to a $L_x = L_y = 30$ box for the three-dimensional simulation changes the value of the growth rate by about 3 %. Since perturbations are usually localized in the core of the vortices and are associated to short-range velocity perturbation, this reduction of the domain for the three-dimensional stability computation has little impact.

In order to make the basic state quasi-steady, the angular velocity of the two vortices around each other has been determined as explained in §2.2. Column 5 of table 1 shows that even if we voluntarily decrease the rotation rate Ω_b by 2 %, i.e. to the rotation rate at the beginning of the two-dimensional simulation Ω_0, the instability growth rate varies only by 2 %. The adjustment between the initial rotation rate Ω_0 and the actual rotation rate Ω_b is therefore important, but not critical for the precision achieved.

Morever, the influence of the initial distance between the two vortices b_0 has been investigated for different basic states with the same value of α_b ($\alpha_b = 0.15$), but taken at different times shown by a filled circle in figure 2. Figure 13 shows that the growth rate is independent to a remarkable extent of the initial distance b_0. This indirectly confirms that the two-dimensional basic state depends only on α_b and can be generated by two-dimensional simulations initialized by different α_0 (Sipp *et al.* 2000; Le Dizès & Verga 2002).

REFERENCES

BATCHELOR, G. K. 1967 *An Introduction to Fluid Dynamics*. Cambridge University Press.

BILLANT, P. & CHOMAZ, J.-M. 2000*a* Experimental evidence for a new instability of a vertical columnar vortex pair in a strongly stratified fluid. *J. Fluid Mech.* **418**, 167–188.

BILLANT, P. & CHOMAZ, J.-M. 2000*b* Theoretical analysis of the zigzag instability of a vertical columnar vortex pair in a strongly stratified fluid. *J. Fluid Mech.* **419**, 29–63.

BILLANT, P. & CHOMAZ, J.-M. 2000*c* Three-dimensional stability of a vertical columnar vortex pair in a stratified fluid. *J. Fluid Mech.* **419**, 65–91.

BILLANT, P. & CHOMAZ, J.-M. 2001 Self-similarity of strongly stratified inviscid flows. *Phys. Fluids* **13**, 1645–1651.

CERRETELLI, C. & WILLIAMSON, C. H. K. 2003 The physical mechanism for vortex merging. *J. Fluid Mech.* **475**, 41–77.

CHO, J. Y. N., JURGENS, R. F. & SLADE, M. A. 1996 High-resolution stratospheric dynamics measurements with the NASA/JPL goldstone solar system radar. *Geophys. Res. Lett.* **23**, 1909–1912.

CHO, J. Y. N. & LINDBORG, E. 2001 Horizontal velocity structure functions in the upper troposphere and lower stratosphere: 1. observations. *J. Geophys. Res.* **106**, 10 223–10 232.

CROW, S. C. 1970 Stability theory for a pair of trailing vortices. *AIAA J.* **8**, 2172–2179.

DALAUDIER, F., SIDI, C., CROCHET, M. & VERNIN, J. 1994 Direct evidence of 'sheets' in the atmospheric temperature field. *J. Atmos. Sci.* **51**, 237–248.

DELBENDE, I., CHOMAZ, J.-M. & HUERRE, P. 1998 Absolute/convective instabilities in the batchelor vortex: a numerical study of the linear impulse response. *J. Fluid Mech.* **355**, 229–254.

DUGAN, J. P. 1984 Towed observation of internal gravity waves and patches of finescale turbulence, in internal gravity waves and small scale turbulence. *Proc. Aha Huliko's Hawaiian winter workshop* (ed. P. Muller & R. Pujalet), pp. 51–64.

EDWARDS, W. S., TUCKERMAN, L. S., FRIESNER, R. A. & SORENSEN, D. C. 1994 Krylov methods for the incompressible Navier–Stokes equations. *J. Comput. Phys.* **110**, 82–102.

ELOY, C. & LE DIZÈS, S. 1999 Three-dimensional instability of Burgers and Lamb–Oseen vortices in a strain field. *J. Fluid Mech.* **378**, 145–166.

FINCHAM, A. M., MAXWORTHY, T. & SPEDDING, G. R. 1996 Energy dissipation and vortex structure in freely decaying, stratified grid turbulence. *Dyn. Atmos. Oceans* **23**, 155–169.

GODEFERD, F. S. & STAQUET, C. 2003 Statistical modelling and direct numerical simulations of decaying stably stratified turbulence. Part 2. Large-scale and small-scale anisotropy. *J. Fluid Mech.* **486**, 115–159.

GREGG, M. C. 1987 Diapycnal mixing in the thermocline: a review. *J. Geophys. Res.* **92**, 5249–5286.

HERRING, J. R. & MÉTAIS, O. 1989 Numerical experiments in forced stably stratified turbulence. *J. Fluid Mech.* **202**, 97–115.

HOLFORD, J. M. & LINDEN, P. F. 1999 Turbulent mixing in a stratified fluid. *Dyn. Atmos. Oceans* **30**, 173–198.

IMBERGER, J. & IVEY, G. N. 1991 On the nature of turbulence in stratified fluid, II, applications to lakes. *J. Phys. Ocean.* **21**, 659–680.

JULIEN, S., ORTIZ, S. & CHOMAZ, J.-M. 2004 Secondary instability mechanisms in the wake of a flat plate. *Eur. J. Mech.* B/*Fluids* **23**, 157–165.

KERSWELL, R. R. 2002 Elliptical instability. *Annu. Rev. Fluid Mech.* **34**, 83–113.

LE DIZÈS, S. & LACAZE, L. 2005 An asymptotic description of vortex Kelvin modes. *J. Fluid Mech.* **542**, 69–96.

Le Dizès, S. & Laporte, F. 2002 Theoretical predictions for the elliptical instability in a two-vortex flow. *J. Fluid Mech.* **471**, 169–201.

Le Dizès, S. & Verga, A. 2002 Viscous interaction of two co-rotating vortices before merging. *J. Fluid Mech.* **467**, 389–410.

Leblanc, S. 2003 Internal wave resonances in strain flows. *J. Fluid Mech.* **477**, 259–283.

Lilly, D. K. 1983 Stratified turbulence and the mesoscale variability of the atmosphere. *J. Atmos. Sci.* **40**, 749–761.

Lindborg, E. 2002 Strongly stratified turbulence: A special type of motion. In *Advances in Turbulence IX, Proceedings of the Ninth European Turbulence Conference*.

Lindborg, E. 2006 The energy cascade in a strongly stratified fluid. *J. Fluid Mech.* **550**, 207–242.

Luce, H., Crochet, M. & Dalaudier, F. 2001 Temperature sheets and aspect sensitive radar echoes. *Ann. Geophys.* **19**, 899–920.

Melander, M. V., Zabusky, N. J. & McWilliams, J. C. 1988 Symmetric vortex merger in two-dimensions: causes and conditions. *J. Fluid Mech.* **195**, 303–340.

Meunier, P., Ehrenstein, U., Leweke, T. & Rossi, M. 2002 A merging criterion for two-dimensional co-rotating vortices. *Phys. Fluids* **14**, 2757–2766.

Meunier, P. & Leweke, T. 2001 Three-dimensional instability during vortex merging. *Phys. Fluids* **13**, 2747–2750.

Miyazaki, T. 1993 Elliptical instability in a stably stratified rotating fluid. *Phys. Fluids* **5**, 2702–2709.

Miyazaki, T. & Fukumoto, Y. 1992 Three-dimensional instability of strained vortices in a stably stratified fluid. *Phys. Fluids* **4**, 2515–2522.

Moore, D. W. & Saffman, P. 1975 The instability of a straight vortex filament in a strain field. *Proc. R. Soc. Lond.* **346**, 413–425.

Muschinski, A. & Wode, C. 1997 First in situ evidence for coexisting submeter temperature and humidity sheets in the lower free troposphere. *J. Atmos. Sci.* **55**, 2893–2906.

Otheguy, P., Billant, P. & Chomaz, J.-M. 2006 The effect of planetary rotation on the zigzag instability of co-rotating vortices in a stratified fluid. *J. Fluid Mech.* **553**, 273–281.

Park, Y.-G., Whitehead, J. & Gnanadeskian, A. 1994 Turbulent mixing in stratified fluids: layer formation and energetics. *J. Fluid Mech.* **279**, 279–311.

Pierrehumbert, R. T. 1986 Universal short-wave instability of two-dimensional eddies in an inviscid fluid. *Phys. Rev. Lett.* **57**, 2157–2159.

Pradeep, D. S. & Hussain, F. 2004 Effects of boundary condition in numerical simulations of vortex dynamics. *J. Fluid Mech.* **516**, 115–124.

Praud, O., Fincham, A. & Sommeria, J. 2005 Decaying grid turbulence in a strongly stratified fluid. *J. Fluid Mech.* **522**, 1–33.

Riley, J. J. & Lelong, M.-P. 2000 Fluid motions in the presence of strong stable stratification. *Annu. Rev. Fluid Mech.* **32**, 617–657.

Riley, J. J., Metcalfe, W. & Weissman, M. A. 1981 Direct numerical simulations of homogeneous turbulence in density-stratified fluids. *Proc. AIP Conf. Nonlinear Properties of Internal Waves* (ed. Bruce J. West), pp. 79–112.

Sipp, D. & Jacquin, L. 2003 Widnall instabilities in vortex pairs. *Phys. Fluids* **15**, 1861–1874.

Sipp, D., Jacquin, L. & Cossu, C. 2000 Self-adaptation and viscous selection in concentrated two-dimensional vortex dipoles. *Phys. Fluids* **12**, 245–248.

Thorpe, S. A. 1977 Turbulence and mixing in a scottish loch. *Phil. Trans. R. Soc. Lond.* A **286**, 125–181.

Thouret, V., Cho, J. Y. N., Newell, R. E., Marenco, A. & Smit, H. G. J. 2000 General characteristics of tropospheric trace constituent layers observed in the mozaic program. *J. Geophys. Res.* **105**, 17 379–17 392.

Tsai, C.-Y. & Widnall, S. E. 1976 The stability of short waves on a straight vortex filament in a weak externally imposed strain field. *J. Fluid Mech.* **73**, 721–733.

Waite, M. & Bartello, P. 2004 Stratified turbulence dominated by vortical motion. *J. Fluid Mech.* **517**, 281–308.

Waleffe, F. 1990 On the three-dimensional instability of strained vortices. *Phys. Fluids* A **2**, 76–80.